

Inclusive production of isotopically resolved Li through Mg fragments by 480 MeV p+Ag reactions

Ray E. L. Green and Ralph G. Korteling

Department of Chemistry, Simon Fraser University, Burnaby, British Columbia, Canada V5A 1S6

K. Peter Jackson

TRIUMF, Vancouver, British Columbia, Canada V6T 2A3

(Received 21 November 1983)

Energy spectra and angular distributions have been measured for 46 isotopically separated Li through Mg fragments produced in reactions of 480 MeV protons with Ag. Thin silicon solid state detectors have been used with time-of-flight techniques to extend measured fragment energies as low as 1 MeV per nucleon, well below the most probable fragment energies. Reasonable fits to the relatively small evaporative components of the spectra are obtained using a self-consistent calculation previously developed. An analysis of the remaining nonevaporative components using contours of relativistically invariant cross section in the plane of rapidity and perpendicular momentum indicates that these components can be described in terms of isotropic emission from moving sources if the source velocity is allowed to be a function of the fragment's radial velocity in the source frame. The relationship between these velocities is essentially independent of fragment Z and A . Coupled with the evaporation calculation, this relationship allows all spectra to be reasonably fit at all angles by use of a simple (four parameters per fragment) phenomenological form for the isotropic nonevaporative component in the moving source frame. While such a form might suggest a statistical origin for the nonevaporative components, detailed consideration of the parameters required suggests difficulties with such an interpretation. Implications of these data for other models are discussed. Energy integrated and total cross sections are calculated.

I. INTRODUCTION

This paper discusses the results¹ of another in a sequence of experiments seeking to characterize the single particle inclusive spectra of helium and heavier fragments produced by the interactions of intermediate energy protons with silver nuclei. Analysis of data from the first experiments,² measuring $\text{Ag}(p, {}^3\text{He})X$ and $\text{Ag}(p, {}^4\text{He})X$ at $E_p = 210, 300,$ and 480 MeV, established that even the prototype fragment for charged particle evaporation, namely ${}^4\text{He}$, had significant nonevaporative components associated with its production. Measurement of heavier fragments from Ag at the same three proton energies³ indicated that a significant portion, probably in fact the majority, of these heavy fragments are from sources other than conventional evaporation from an excited residual nucleus left behind by earlier rapid processes. A third experiment⁴ sought possible support for some of the direct interaction theories (for example, Refs. 5–7, and others reviewed in Ref. 8) proposed to explain the nonevaporative fragments. It sought this support by looking for polarization effects associated with helium fragment production but found instead, in contrast to the proton emission case,^{9,10} no significant analyzing powers associated with these spectra. (For general review of previous work in this field see in particular Refs. 3 and 11–13.)

For protons incident on medium mass nuclides such as silver, previous work has left important aspects of the fragment single particle inclusive spectra yet to be adequately characterized. The experiments reported here ex-

tend our measurements into some of these inadequately defined regions. In particular, the work reported here had three principal experimental objectives. The first was isotopic separation of the heavier fragments at both low and high fragment energies. Our previous measurements resolved fragments of $Z > 4$ only by element, while the present experiment provides isotopically separated spectra for all fragments through Mg. The second experimental objective was a more complete definition of the fragment angular distributions. Our previous work provided a coarse three point distribution adequate for some types of analysis, while the present experiment provides a more detailed distribution with six principal angles plus some supplemental measurements at other angles. The third experimental objective was a more detailed characterization of the spectra for heavy fragments of low energies. Previous work has used targets whose thickness causes a significant distortion of these low energy portions of the spectra. The present work minimizes these distortions by using targets of $\approx 200 \mu\text{g}/\text{cm}^2$ thickness.

One characteristic of these fragment spectra, well established by our previous measurements, is the relative insensitivity of all of their features, except overall magnitude, to the incident proton energy. We have thus chosen to use only the one incident beam energy of 480 MeV for the work reported here. The expectation is that any conclusions drawn from the work may be extended to a significant range of incident proton energies.

The desire to extend the measurement of isotopically resolved fragments to B through Mg is motivated by

several factors. From a purely experimental point of view, there are significant differences in spectral shape between isotopes of a given element for the lower Z fragments and it is of interest to see if this persists as the atomic number of the fragment increases. From a more model-specific perspective, relative isotopic yields can be an important input to some calculations. At high fragment energies, for example, some of the data reported here have already been needed in a preliminary form to assess the merits of a snowball model⁷ for fragment production. To remain as credible descriptions, all models of nonevaporative fragment emission must eventually be extended to these heavy fragments and compared with experiment. References 3 and 14 point out the value of isotopically separated low energy data in evaluating the contribution of evaporation to the measured spectra. It is particularly useful to have low energy data on several isotopes of a given element for as many elements as possible. This allows evaluation of evaporation models without some of the uncertainties stemming from the inverse cross section portion of the calculation.

Study of the angular dependence in greater detail is motivated principally by the desire to confirm the smooth behavior previously assumed. Available experimental results do not lead one to expect any dramatic changes in the spectra over small angular increments, but there exist models which predict such rapid changes, e.g., quasifree scattering or shock-wave models in some of their versions. Experimental confirmation that the angular dependence is indeed smooth is thus a useful check on such models. Finer angular increments also allow a more accurate angular integration to obtain total production cross sections. Of direct interest in terms of our previous work^{2,3} are the shapes of the contours of invariant cross section $(1/p)(d^2\sigma/d\Omega dE)$ in the plane of p_{\perp}/mc vs y where p_{\perp} , m , and y are, respectively, the perpendicular component of the fragment's momentum, its mass, and its rapidity. Analysis of our three point distributions, as well as analysis¹⁵ of three point distributions from higher energy work,¹⁶ have shown that contours appropriate to isotropic emission from sources moving in the beam direction fit the extant data for fragments of $A > 3$ as long as the source velocity is allowed to be a function of contour level. The finer angular increments used in the work here confirm that such fits are indeed appropriate although the significance of this result is not entirely clear.

Accurate definition of the low energy parts of the spectra is useful in determining parameters for evaporation calculations and also, presumably, for determining those of nonevaporative calculations once such models are extended to include the low-energy region. In particular, this information is required in order to determine the appropriate Coulomb barrier associated with these fragment spectra. Literature values for the Coulomb barrier, reported as a fraction of the barrier thought appropriate for the target nucleus, vary from near 1.0 to values as low as 0.3. While most of this variation is more dependent on the calculations than the data, accurate data should be available in the advent of an accurate calculation.

In order to obtain the desired data, silicon surface barrier detectors have been used in standard compact detector

telescopes and in detector telescopes which include 50 cm flight paths between the first and second detectors. Time-of-flight (TOF) information in the separated telescopes provided the improved mass resolution desired for this work. Previously used $\Delta E, E$ techniques provided Z identification for both types of telescopes as well as isotopically separated Li, Be, and high energy B fragment spectra for data from the compact telescopes. The lower bound on the energies of the heavier fragments was reduced to approximately 1 MeV per nucleon by use of a 7.3 μm thick ΔE detector. Details of the experimental techniques used in this work are discussed in the next section, followed by sections describing the results and analysis of the results.

II. EXPERIMENTAL TECHNIQUES

The experimental work was conducted using a 152 cm diameter scattering chamber located in an external proton beam line at the TRIUMF cyclotron. The electronics and data acquisition systems were in an equipment trailer approximately 40 m away. Off-line data reduction was performed at the Simon Fraser University Computing Centre. Those aspects of the experiment associated with operation of the compact detector telescopes are essentially identical to those described in Ref. 3 and earlier work^{2,17} and will not be discussed in detail here. Instead we will concentrate on new aspects associated with the TOF telescopes and the thin targets.

A. The TOF telescopes

Two basic TOF telescopes composed of commercial silicon surface barrier detectors were used. The first telescope had a 7.3 μm ΔE detector (10 mm² active area) and was used in conjunction with thin targets to achieve accurate definition of the spectra at low fragment energies. The second telescope used a 20.5 μm ΔE detector (25 mm² active area) in conjunction with somewhat thicker targets to define the higher energy portions of the spectra. In both cases, the ΔE detectors were immediately behind a 1 mm thick copper collimator with an inner diameter defining an area somewhat smaller than the active area of the detector (2.5 and 5 mm diameters, respectively). This collimator was 15 cm from the center of the target. The stopping (E) detector of both telescopes was 50 cm beyond the ΔE detector and was immediately preceded by a 10 mm inner diameter by 1 mm thick Cu collimator. It was followed by a reject detector to provide a veto signal for particles which failed to stop in the second detector. Various stopping and reject detectors were used depending on the particular portion of the data being collected. The stopping detectors had 100 mm² active areas and ranged in thickness from 250 to 500 μm . Reject detectors had 150 mm² active areas and were approximately 200 μm thick. All detectors, including the 7.3 μm unit, were cooled to approximately 0°C during experimental runs by use of Peltier junctions. This cooling reduced the detector reverse currents dramatically and allowed full operating bias voltages to be easily maintained at the detectors.

The preamplifiers for the ΔE and stopping detectors were operated inside the vacuum chamber and were con-

nected to the detectors with short (≈ 10 cm) cables to minimize input capacitance. These commercial preamplifiers were equipped with a built-in time pickoff circuit and provided a fast signal with rapid decay time in addition to the normal energy signal with slow decay time. The adjustment available on these preamplifiers was used to optimize the fast timing signal for each input capacitance used. Energy calibrations for each detector-preamplifier combination were obtained by the means described in Ref. 3. During data collection, pulser signals were processed concurrently at 1 Hz to monitor energy and timing stability. No problems were encountered in the stability of these systems.

Energy signals from the TOF telescopes were processed in a similar manner to those of the compact telescope, and this has been treated in detail in Ref. 3. The only significant differences were the resolving time for the $\Delta E, E$ coincidence and the additional use of the event signal to gate an analog TOF signal into an analog-to-digital converter (ADC) unit of the data acquisition system. The coincidence resolving time used was typically 300 ns in order to allow the slow moving fragments time to traverse the 50 cm flight path. The increased accidental coincidences incurred by this long resolving time were not a problem because the TOF information was used to exclude them.

Timing signals from the TOF preamplifiers were carried out on 50 Ω fast signal cables (FM8) to well-terminated inputs on fast amplifiers in the equipment trailer. High quality terminations allowed use of wide dynamic signal ranges without false triggers from reflected signals. Outputs from the amplifiers were processed in constant fraction discriminator (CFD) units whose outputs were used as inputs to a time-to-amplitude converter (TAC) unit. The CFD output signal rates for the ΔE systems were considerably lower than the stopping detector rates and so the ΔE signals were used to start the TAC. The ADC which digitized the TAC output was calibrated by using a pulser signal split into the ΔE and E systems. A series of 20 ns delays was inserted in the TAC stop signal input line and the centroids of the peaks in the subsequent spectra were fit to a linear calibration by a least-squares procedure. During data runs, the TAC output was gated into its ADC whenever the logic system associated with the energy signals indicated a valid event had occurred. The ΔE , E , and TAC output values from their respective ADC units were then recorded by the data acquisition system event by event on magnetic tape. Overall time resolution depended strongly on the combination of ΔE and E energies involved; typical values ranged from 200 ps to 1 ns with the fortunate combination of long flight times with poor time resolution.

The particle identification algorithm of Ref. 3, a modified version of an earlier algorithm,¹⁷ was used in an offline analysis to identify the atomic number Z of fragments measured in the TOF systems. Figure 1 shows an example of this identification for the 7.3 μm ΔE system. The data for each group of fragments associated with a given Z were then processed in subsequent programs which provided mass identification for these fragments. For a given Z , the data were processed such that an in-

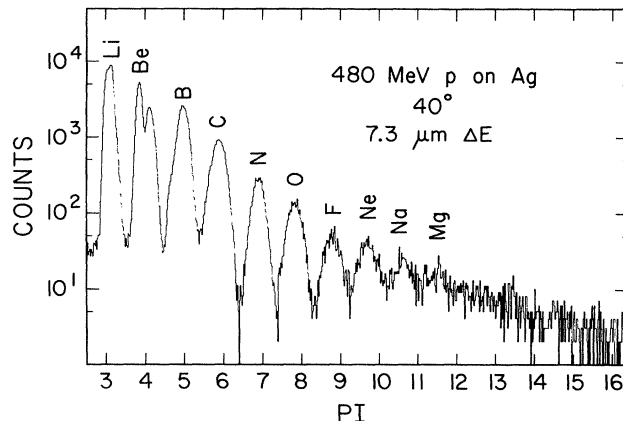


FIG. 1. Fragment particle identification spectrum obtained by applying the algorithm of Ref. 3 to data from a TOF telescope with a 7.3 μm ΔE detector. Subsequent analysis of the time information yields fragment masses. The thin Ag target used in obtaining this data had a VYNS backing which is a major contributor to the light proton-rich fragments such as ^7Be .

teractive graphics program displayed numbers of counts on a two-dimensional grid of E (calibrated in MeV) versus a time (in ns) equal to the recorded TOF time minus a flight time calculated from E assuming an atomic mass number of $A=2Z$. Regions were then defined on this grid using the interactive features of the program and data inside each of these regions were assigned to given fragment types. For each data point in a region, values for the total fragment energy $\Delta E + E$ were accumulated in histograms to yield raw energy spectra, i.e., the unnormalized spectra not yet corrected for multiple scattering in the ΔE detector or for target effects.

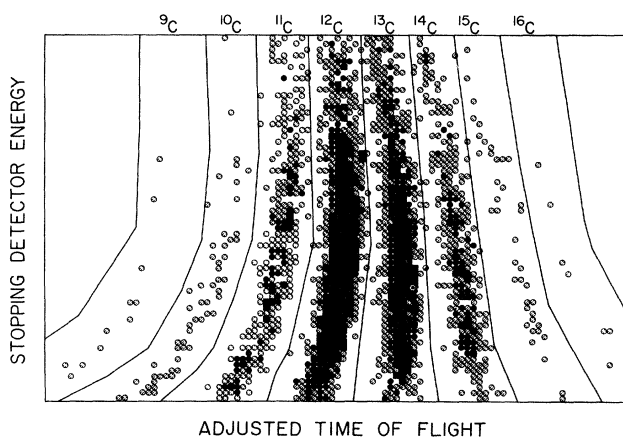


FIG. 2. Stopping detector energy versus measured time of flight minus the calculated ^{12}C time of flight based on the stopping energy. The fragment Z has previously been selected using $\Delta E, E$ analysis. Data are from a TOF telescope with a 7.3 μm ΔE detector and for fragments at 90° from a thin Ag target with a VYNS backing. Cells containing more than six counts are shown as dark squares, those with four to six counts as dark circles, and those with one to three counts as light circles. Regions used to define the various masses are also shown; these were determined by examining data from all angles measured with equivalent detector telescope parameters.

Figure 2 shows an example of the type of data treated in the interactive graphics program, as well as the regions defined for this data by use of the program. For Be and B fragments analyzed in this program, assignment of data to fragment type is trivial because of the absence of ^8Be and ^9B fragments. For $Z > 5$, identification of the $A = 2Z$ isotopes, and hence the others, was possible because the Be and B isotope data could be used to define the expected time domain ($t = 0$ in a perfect system with no offset in the start and stop signals) for these isotopes. For sufficiently energetic ΔE and E signals, the CFD units performed well enough to allow unambiguous assignments of the $A = 2Z$ isotope for all Z studied. Variations in the $A = 2Z$ times from one Z to the next were typically only 10% of the time spacing between adjacent A values.

Where reasonable statistics exist, errors from incorrectly defining the appropriate regions are considerably smaller than our errors in relative normalizations. For cases with low cross sections, accurate definition of the appropriate regions is not as good, although such identification is aided by systematics and the independence of region from detector angle. For the Ne, Na, and Mg fragments, the Z identification at low energies also deteriorates somewhat. Contributions from these effects range from at most a few percent for the common lighter isotopes to perhaps $\pm 50\%$ for the extreme cases of the heaviest or lightest isotopes of F through Mg.

B. Multiple scattering corrections

Separating the ΔE and E detectors to obtain a flight path for the TOF measurements leads to an energy dependent inefficiency in fragment detection due to the multiple scattering of the fragments in the ΔE detectors. There are also difficulties in accurately defining the geometries of these separated telescopes since they depend on the details of the beam profile on the target. To correct for these inefficiencies, we compared elementally separated data from the compact $\Delta E, E$ telescopes to the sum for each element of the isotopically separated data from the TOF telescopes. The compact telescopes had well-defined geometries and detected fragments above their energy thresholds in the telescopes with essentially unit efficiency. The comparison of the TOF data with this data thus allowed extraction of cross sections from the TOF data in spite of the difficulties with detection efficiencies. The remainder of this subsection discusses details of these efficiency corrections.

Multiple scattering theory for thin targets¹⁸ suggests that the efficiency correction should be a function of the kinetic energy of the fragment divided by its atomic number with no other dependence on the fragment parameters. Within the statistical accuracy of our data, we observed that this was indeed true. We thus sought a function $g(E/Z)$ which fit our observed efficiencies for elementally separated fragments and which then was used to correct the isotopically separated TOF data. For this correction, we took E to be the energy of the fragment as incident on the telescope. (In thin target multiple scattering theory, the change in energy as the fragment passes through the target is neglected. We found that a simple modification to the theory was sufficient to correct it for

our use where E is noticeably reduced in passing through the first detector.) The function $g(E/Z)$ can be factored into an overall normalization depending on geometry alone (the efficiency for unscattered fragments, i.e., in the limit of large E/Z) and a function $f(E/Z)$ which gives the effects of multiple scattering and its coupling with geometry. Determining the overall normalization was straightforward using the comparisons already discussed, and the remainder of this section discusses only $f(E/Z)$.

Within thin target theory, the form of $f(E/Z)$ may be calculated for the idealized case of a pencil beam incident on the first detector (thickness t) along an axis passing through the center of the stopping detector. If the stopping detector is a distance R beyond the initial detector and is sensitive to fragments within a circle of radius a about the axis, the fraction of incident particles detected by the stopping detector is

$$[f(E/Z)]_{\text{ideal}} = 1 - \exp \left[-\frac{c}{t} \left(\frac{a}{R} \right)^2 \left(\frac{E}{Z} \right)^2 \right], \quad (1)$$

where c is a number which depends on the material in the incident detector.

In our nonideal case, the coupling of geometry and multiple scattering modify somewhat the way $f(E/Z)$ approaches unity as $E/Z \rightarrow \infty$. At low E/Z where the mean square scattering angle $\langle \theta^2 \rangle \gg (a/R)^2$, our actual geometry should yield the same results as the idealized geometry, i.e., $f(E/Z) \propto (E/Z)^2$, except for effects due to the change in energy as a fragment traverses the scattering medium. By using for low E/Z a form

$$f(E/Z) \propto [(E/Z) - b]^2$$

where b is a constant chosen to compensate for the finite thickness of the initial detector, we were able to obtain reasonable fits to the measured efficiencies. For the TOF telescope using the $7.3 \mu\text{m}$ ΔE detector, it was important to use a physically reasonable form for the efficiency at low E/Z since the companion compact detector telescope used a $12.9 \mu\text{m}$ ΔE detector and thus the efficiency correction at the lowest E/Z values had to be extrapolated from higher E/Z measurements. The efficiency correction used for the $7.3 \mu\text{m}$ ΔE TOF telescope was

$$f \left(\frac{E}{Z} \right) = 0.02766 \left(\frac{E}{Z} - 0.26746 \right)^2, \quad \text{for } \frac{E}{Z} \leq 3.7 \quad (2)$$

$$= 1.0 - \exp \left\{ - \left[\left(\frac{E}{Z} - 3 \right) / 4.5 \right]^{1/2} \right\},$$

$$\text{for } \frac{E}{Z} > 3.7,$$

where the form at high E/Z is merely an empirical fit to the data. This correction is plotted in Fig. 3 along with the elemental data for B, C, and N fragments from one of the experimental runs. The curve extends down in E/Z to the lowest value used in correcting data presented in this paper.

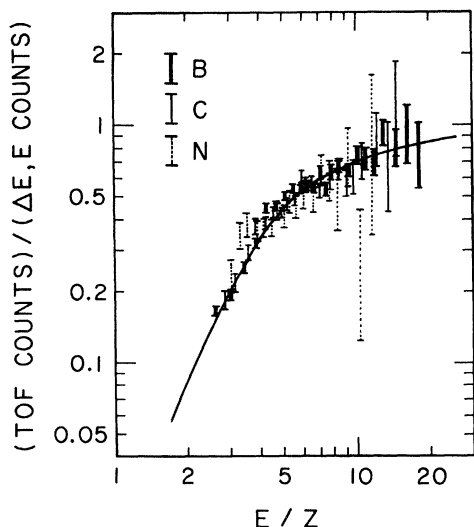


FIG. 3. The ratio of counts from a TOF telescope with a $7.3 \mu\text{m}$ detector to counts from a compact $\Delta E, E$ telescope at the same angle from the beam as a function of fragment energy (in MeV) divided by fragment atomic number. (The values have been scaled such that the ratio is for the case where both telescopes subtend the same solid angle at $E/Z = \infty$.) The data shown are for one run with the telescopes at 90° . Also shown is the function used to correct the TOF data for multiple scattering in the ΔE detector.

C. Targets

The primary targets used for these measurements were natural silver either evaporated onto VYNS (85% CH_2CHCl and 15% $\text{CH}_3\text{CO}_2\text{CHCH}_2$) films or in the form of thin free standing foils. They were 6 cm high by 8 cm wide. The free standing foils were of thicknesses around 2 mg/cm^2 and the evaporated targets were typically 200 to $300 \mu\text{g/cm}^2$ of Ag on 80 to $160 \mu\text{g/cm}^2$ of VYNS. Normalizations were determined by means which did not rely on knowledge of the target thickness. Thicknesses were used to provide minor corrections to the final energy values used for some of the fragment spectra.

Secondary targets of pure VYNS were used to measure background spectra for the backing on the thin Ag targets (and as an approximation to the background from contaminants on the thicker foils). The shapes of these background spectra differ dramatically from the spectra due to a pure Ag target; for the thin targets, the spectra for neutron deficient isotopes of $Z < 7$ at the lowest fragment energies measured are completely dominated by the background spectra. By using this information (with a redundancy due to the several isotopes in this category), consistent corrections could be made for the relative yields from the VYNS on the thin Ag targets. In many cases, the lowest fragment energies meaningfully measured were limited by the statistical errors in the spectra obtained by subtracting the background from the target-plus-backing measurements. Meaningful thin target measurements of ^8B and ^{10}C were entirely precluded by the large background contributions in these spectra. Figure 4 shows the background contribution for a typical case where it is important but not dominant.

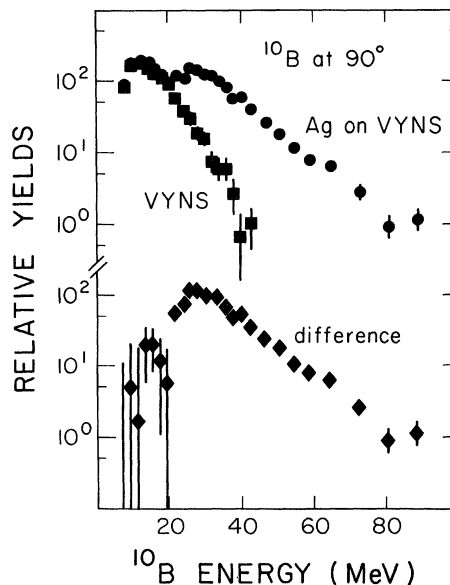


FIG. 4. An example of the background from the VYNS backing on the thin Ag targets and its effects on the raw spectra used as input to further analysis.

In general, the thicker target foils were used in conjunction with the $20.5 \mu\text{m}$ ΔE TOF telescope to define the higher energy portions of the fragment spectra, while the thinner targets were used with the $7.3 \mu\text{m}$ system to define the lower energy portions of the spectra. In order to combine these spectra and for convenience in using the spectra, the measured fragment energies for all runs using the free standing foils have been corrected to account for the energy loss in the target under the assumption that the fragments originate in the midplane of the foil. The size of such a correction for the thin targets was not significant enough compared to the uncertainties involved to justify its use. In effect, the spectra presented in this paper are those one expects from a thin silver target of $200 \mu\text{g/cm}^2$, with uncertainties in fragment energy of $\pm 2\%$ or an amount corresponding to a thickness uncertainty of $\pm 200 \mu\text{g/cm}^2$, whichever is larger.

D. Normalizations

Due to the length of time over which these experiments were run plus the accidental destruction of several of the delicate targets, many different combinations of targets and beam monitors are involved in the normalization of the data presented here. However, during each set of experimental runs there was at least one good beam monitor system (and frequently two) functioning and at least one run from an experimental configuration for which previously normalized data³ were available. This allowed all of the data to be absolutely normalized to $\pm 30\%$. The relative internal normalization between angles should be good to $\pm 10\%$.

The compact telescope data from the thick target runs provided fertile grounds for testing our normalization procedures since there were several nearly independent sources for the normalizations. Among these were moni-

tor telescope values using the calibrations from Ref. 3, comparisons of integrated fragment spectra to previous³ normalized data, comparisons of integrated fragment spectra to the normalized thin target data of the present measurements, and relative values using the secondary-emission monitor (SEM). The values we adopted were selected in an effort to minimize the propagation of errors affecting relative normalizations. All comparisons of alternate normalizations to these adopted values fall within 13% of the adopted value (approximately half within 5%) except one case (at 160°) which disagreed by 17%.

The higher energy portions of the various compact telescope spectra at 10° represent only lower limits on the cross sections because the energy rate from background events in the final stopping detector may on occasion have forced the preamplifier base voltage level beyond the operating range of the amplifier used.

III. RESULTS

The data resulting from the measurements reported in this paper are tabulated in the Physics Auxiliary Publication Service of The American Institute of Physics (AIP).¹ The statistical error in each point is tabulated but no estimates of systematic errors in identification or in the multiple scattering or target corrections are included in the tabulation nor are errors in the normalizations included. These statistical errors are the ones shown in the sample fragment energy spectra displayed in this paper.

Tables I–III summarize the range of data taken in this study and available in the tabulation. These tables have either two or three entries for each combination of fragment type and angle of emission from the 480 MeV p + Ag reactions summarized. The first entry, of the form *bb-tt*, indicates data are tabulated for the given fragment and angle between energies of *bb* MeV and *tt* MeV. The second entry is the integral

$$\left(\frac{d\sigma}{d\Omega} \right)_{\text{meas}} = \int_{bb}^{tt} \frac{d^2\sigma}{d\Omega dE} dE \quad (3)$$

of the cross section between the lowest and highest fragment energies tabulated, in $\mu\text{b}/\text{sr}$. The errors given are statistical only. The third entry, when present, is a number indicating our estimate (from analysis described later) of the total value for $d\sigma/d\Omega$, in $\mu\text{b}/\text{sr}$. As discussed earlier, the overall normalizations for these integrated values are believed known to $\pm 30\%$, while the relative normalizations between angles are believed known to $\pm 10\%$, except perhaps the 10° data in Table I as already discussed. For the third entries, we include our 10% error in relative normalization as well as our estimate for errors in the extrapolation and in identification of the low cross section isotopes.

The energy limits on the data stem from varied causes, leading to the seemingly unsystematic variation as the observed isotope or angle is varied. The basic lower energy limit is determined by the requirement that the range of the fragment be sufficient for it to pass through the first detector and consistently deposit sufficient energy in the second detector to trigger the logic electronics. While this limit is sometimes obtained, it is often exceeded by the

limit from decreasing statistical accuracy as the fragment energy decreases due to the increasing contribution from background sources and/or the decreasing cross section for fragment production. The decrease in efficiency with decreasing fragment energy in the TOF telescopes, caused by the multiple scattering in the first detector, exacerbates the statistical problem. The $\Delta E, E$ data of Table I for compact telescope measurements with the approximately 2 mg/cm² Ag foil targets has even further limits on the lower energies. For the ^{8,9}Li, ¹¹Be, and all B fragments, the particle identification is not adequate to separate these from neighboring isotopes until the fragments have sufficient range to trigger the third detector of the four or five element telescopes used. For part of the runs, the electronic logic used to reject light fragment events from being presented to the computer and swamping the analysis system (the Σ system of Ref. 3) was inadvertently set at a level which rejected some of the low energy Li and Be fragments.

The upper energy limits are most frequently due to the cross section having fallen below levels measurable with the statistical accuracy of these experiments. In some cases (notably ^{6,7}Li and ⁷Be), the limits are at energies where the fragments have passed through the last data detector and into or through the final veto detector which all telescopes contained. Variations for these latter cases are due to the fact that the stopping detectors used in the telescopes were not always the same thickness.

The TOF data of Table II are the combined thick target and thin target data. The low energy portions are strictly from the thin target runs. For the higher energies, the thick target data have been corrected for target thickness and then matched with the thin target data to extend it to higher energies. For F through Mg fragments, only thin target data have been used.

Table III summarizes the data, separated by element only, measured for the approximately 200 $\mu\text{g}/\text{cm}^2$ targets using the compact detector telescopes. These data do not have the isotopic resolution available in the TOF data, but neither do they have the possible systematic errors stemming from the efficiency correction required for multiple scattering in the TOF telescopes. Examples of the spectra are given in the next section in conjunction with various analyses of the data.

IV. ANALYSIS AND DISCUSSION

A. Two-component fits to individual energy spectra

In order to facilitate further analysis of the data, it is convenient to have smooth fits to the individual single particle inclusive energy spectra. For much of the data presented in this paper, we have achieved reasonable fits of this type with essentially the same procedures used in our earlier work.³

In these fits, the first contribution to each spectrum is taken to be that from the evaporation of fragments from fully equilibrated residual nuclei. The calculation is described in detail elsewhere.¹⁴ Previous ⁴He ejectile data^{2,3} were again used to constrain the description of the emitting system since data for fragments of $Z > 2$ alone

TABLE I. The range of measurements made using $\Delta E, E$ particle identification and approximately 2 mg/cm² Ag targets. For each combination of fragment-type and angle of emission, the first entry gives the minimum and maximum values of the fragment energy (in MeV) for which $d^2\sigma/d\Omega dE$ is tabulated in the compilation (Ref. 1) associated with this paper. The second entry is the integral of the data between the energies specified by the first entry, in $\mu\text{b}/\text{sr}$. The error specified in the second entry is the statistical error only. The third entry, when present, is our estimate of the total value for $d\sigma/d\Omega$, in $\mu\text{b}/\text{sr}$. It is based on an analysis described in the text and the error quoted includes our estimates for all sources of relative error between entries.

| Fragment | Angle | | | | | | | | |
|------------------|-----------|----------------------|----------------------|----------------------|----------------------|----------------------|----------------------|----------------------|----------------------|
| | 10° | 20° | 40° | 60° | 65° | 70° | 90° | 120° | 160° |
| ⁶ Li | 24-92 | 10-140 | 18-116 | 18-116 | 14-140 | 14-140 | 10-140 | 10-140 | 10-124 |
| | 345±1 | 542±3 546±55 | 377±1 421±44 | 322±1 343±35 | 395±2 409±41 | 388±2 404±41 | 274±1 275±28 | 204±1 205±21 | 135±1 135±14 |
| ⁷ Li | 26-108 | 12-148 | 18-132 | 18-132 | 14-148 | 14-148 | 8-140 | 8-124 | 8-116 |
| | 324±1 | 606±3 611±61 | 439±1 486±51 | 386±1 424±44 | 431±2 451±46 | 421±2 443±45 | 302±1 302±30 | 227±1 228±23 | 157±1 157±16 |
| ⁸ Li | 26-132 | 26-148 | 26-140 | 26-140 | 26-148 | 26-140 | 26-124 | 26-124 | 26-92 |
| | 46.3±0.4 | 54.2±0.9 | 38.9±0.3 | 31.5±0.2 | 27.7±0.4 | 25.8±0.4 | 14.9±0.2 | 7.4±0.1 | 3.2±0.1 |
| ⁹ Li | 28-132 | 28-132 | 28-132 | 28-140 | 28-108 | 28-100 | 28-108 | 28-92 | 28-84 |
| | 7.0±0.2 | 8.2±0.3 | 5.9±0.1 | 4.5±0.1 | 3.9±0.2 | 3.1±0.1 | 1.9±0.1 | 0.99±0.03 | 0.45±0.02 |
| ⁷ Be | 34-148 | 12-196 | 16-180 | 16-172 | 20-156 | 20-172 | 12-164 | 12-108 | 12-108 |
| | 63.9±0.5 | 123.9±1.7 124±13 | 103.4±0.4 105±11 | 88.3±0.4 90±9 | 90.3±0.8 101±11 | 85.9±0.7 94±10 | 55.4±0.5 55±6 | 44.8±0.2 45±5 | 26.1±0.6 26±3 |
| ⁹ Be | 18-156 | 18-172 | 18-164 | 18-148 | 18-156 | 18-132 | 12-116 | 12-100 | 12-84 |
| | 100.8±0.6 | 122.9±1.4 126±13 | 88.5±0.4 94±10 | 75.4±0.3 83±9 | 90.7±0.8 97±10 | 89.3±0.7 96±10 | 73.9±0.4 75±8 | 53.1±0.2 54±5 | 40.7±0.3 43±4 |
| ¹⁰ Be | 20-156 | 16-148 | 16-148 | 16-148 | 14-116 | 14-116 | 14-108 | 14-92 | 14-76 |
| | 61.1±0.5 | 61.1±1.0 61.6±6.2 | 57.3±0.3 57.8±5.8 | 52.6±0.3 53.3±5.3 | 41.0±0.5 41.3±4.2 | 39.1±0.4 39.4±4.0 | 26.8±0.2 27.0±2.7 | 23.6±0.1 24.1±2.4 | 12.4±0.1 12.6±1.3 |
| ¹¹ Be | 44-124 | 40-84 | 40-124 | 40-132 | 40-76 | 40-92 | 40-92 | 40-56 | 40-52 |
| | 0.77±0.05 | 0.87±0.11 | 0.79±0.04 | 0.51±0.03 | 0.30±0.04 | 0.34±0.04 | 0.18±0.02 | 0.041±0.006 | 0.030±0.006 |
| ⁸ B | 44-116 | 44-140 | 44-116 | 44-116 | 44-124 | 44-124 | 44-100 | 44-84 | 44-84 |
| | 2.50±0.10 | 2.23±0.19 | 1.11±0.04 | 0.79±0.03 | 0.85±0.07 | 0.63±0.06 | 0.35±0.03 | 0.16±0.01 | 0.05±0.01 |

TABLE I. (Continued).

| Fragment | Angle | | | | | | | |
|-----------------|--------------------|--------------------|--------------------|---------------------|---------------------|---------------------|---------------------|----------------------|
| | 10° | 20° | 40° | 60° | 70° | 90° | 120° | 160° |
| ¹⁰ B | 52-116 11.8±0.2 | 52-148 12.7±0.4 | 52-116 7.5±0.1 | 52-116 5.2±0.1 | 52-124 4.5±0.2 | 52-116 1.9±0.1 | 52-100 0.59±0.02 | 52-92 0.12±0.01 |
| | 52-124 15.5±0.2 | 52-140 17.3±0.5 | 52-124 10.4±0.1 | 52-124 7.0±0.1 | 52-124 5.1±0.2 | 52-108 2.3±0.1 | 52-108 0.60±0.02 | 52-84 0.15±0.01 |
| ¹² B | 52-124 2.4±0.1 | 52-132 2.9±0.2 | 52-124 2.1±0.1 | 52-124 1.37±0.04 | 52-108 0.66±0.06 | 52-116 0.26±0.02 | 52-76 0.08±0.01 | 52-76 0.019±0.005 |

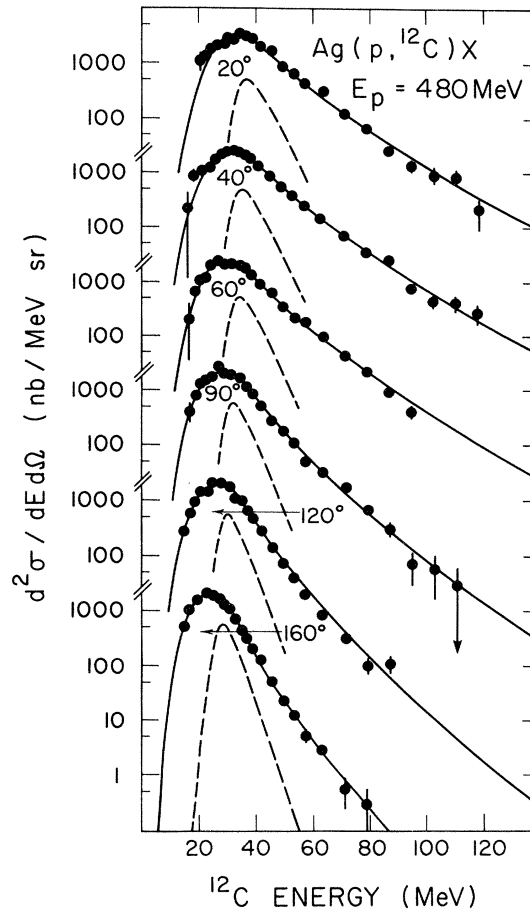


FIG. 5. Energy spectra of ¹²C fragments at six laboratory angles. Fits described in Sec. IV A are also shown; parameters for the nonevaporative component are determined separately at each angle, while the evaporative component (dashed curves) is determined at all angles by one set of parameters.

are not sufficient to define meaningful evaporation parameters. As noted previously, the attempt to achieve self-consistent fits to this component, i.e., a uniform description of the evaporating system independent of the evaporated fragment, indicated that evaporation from fully equilibrated nuclei is not the dominant component in these spectra and that it appears to be even less important as the fragment Z increases.

The second component was again arbitrarily fit to the remaining parts of the spectra using parameters varied freely between angles and fragment types. The functional form for this component had the qualitative features of that used before³ but was of closed analytic form to facilitate automated chi-square searches to find the parameter values. The form used is identical to that described later in connection with more global fits except that fragment momentum instead of energy was used as the independent variable since better fits were then achieved. For the purposes of the fits in this part of the analysis, the important features of the form chosen are that it yields reasonable fits to the data, that it goes monotonically to zero as the fragment energy decreases below its most probable value, and that it falls off exponentially at high fragment

TABLE II. The range of measurements made using time-of-flight mass identification and approximately 0.2 mg/cm² Ag targets. The meanings of the entries are described in the caption for Table I.

| Fragment | Angle | | | | | |
|-----------------|------------|----------|----------|----------|----------|-----------|
| | 20° | 40° | 60° | 90° | 120° | 160° |
| ¹⁰ B | 24–116 | 20–140 | 20–124 | 20–124 | 12–92 | 14–76 |
| | 62.5±2.0 | 48.8±1.4 | 43.8±1.4 | 30.9±0.9 | 27.5±0.8 | 18.4±0.5 |
| | 66.7±7.1 | 49.6±5.2 | 45.7±4.8 | 32.4±3.4 | 27.5±2.9 | 18.6±1.9 |
| ¹¹ B | 18–124 | 16–140 | 14–124 | 12–124 | 12–92 | 12–84 |
| | 125.1±2.8 | 93.5±1.8 | 81.8±2.1 | 65.1±1.6 | 47.8±0.6 | 34.2±0.8 |
| | 125.7±12.9 | 93.8±9.6 | 82.1±8.5 | 65.2±6.7 | 48.0±4.8 | 34.5±3.5 |
| ¹² B | 20–116 | 16–124 | 14–124 | 12–108 | 12–84 | 12–68 |
| | 16.4±0.6 | 12.8±0.4 | 12.7±0.5 | 9.2±0.4 | 6.8±0.2 | 5.4±0.3 |
| | 17.0±1.8 | 12.9±1.3 | 12.7±1.4 | 9.2±1.0 | 6.9±0.7 | 5.5±0.6 |
| ¹³ B | 18–108 | 16–108 | 16–56 | 14–84 | 14–76 | 14–56 |
| | 3.3±0.3 | 2.3±0.1 | 1.8±0.2 | 1.5±0.2 | 1.1±0.1 | 0.82±0.10 |
| | 3.4±0.4 | 2.4±0.3 | 1.8±0.3 | 1.5±0.2 | 1.1±0.2 | 0.90±0.15 |
| ¹¹ C | 28–116 | 26–124 | 24–100 | 24–108 | 16–84 | 16–76 |
| | 13.4±1.0 | 9.0±0.5 | 8.9±0.7 | 6.1±0.3 | 5.2±0.2 | 3.6±0.2 |
| | 13.7±1.7 | 9.2±1.1 | 9.0±1.1 | 6.6±0.8 | 5.3±0.6 | 3.7±0.4 |
| ¹² C | 20–124 | 16–124 | 16–100 | 16–116 | 14–92 | 14–84 |
| | 77.5±1.8 | 60.3±1.0 | 53.2±1.1 | 41.8±0.9 | 34.8±0.6 | 29.3±0.7 |
| | 78.3±8.1 | 60.5±6.1 | 53.4±5.5 | 42.1±4.3 | 35.0±3.6 | 29.9±3.1 |
| ¹³ C | 20–124 | 16–124 | 16–100 | 16–108 | 12–84 | 12–84 |
| | 54.5±1.2 | 42.4±0.7 | 36.4±0.9 | 28.7±0.7 | 23.4±0.5 | 19.8±0.6 |
| | 54.9±5.6 | 42.5±4.3 | 36.6±3.8 | 29.0±3.0 | 23.5±2.4 | 19.9±2.1 |
| ¹⁴ C | 18–108 | 16–100 | 16–100 | 16–84 | 12–76 | 14–76 |
| | 18.7±0.7 | 14.3±0.4 | 13.2±0.5 | 9.6±0.4 | 8.5±0.3 | 7.0±0.4 |
| | 18.8±2.0 | 14.4±1.5 | 13.2±1.4 | 9.8±1.1 | 8.5±0.9 | 7.7±0.9 |
| ¹⁴ N | 22–108 | 16–116 | 16–100 | 16–84 | 12–84 | 14–68 |
| | 19.8±0.8 | 15.6±0.5 | 13.3±0.6 | 10.0±0.5 | 8.8±0.3 | 6.9±0.4 |
| | 20.0±2.1 | 15.6±1.6 | 13.3±1.5 | 10.1±1.1 | 8.8±0.9 | 7.0±0.8 |
| ¹⁵ N | 16–116 | 16–148 | 12–100 | 16–108 | 12–92 | 12–76 |
| | 37.6±1.3 | 29.6±0.6 | 25.5±0.9 | 20.2±0.7 | 16.2±0.4 | 14.0±0.6 |
| | 37.7±4.0 | 29.7±3.0 | 25.6±2.7 | 20.7±2.2 | 16.2±1.7 | 14.1±1.5 |
| ¹⁶ N | 26–92 | 20–100 | 16–92 | 16–76 | 16–68 | 14–40 |
| | 4.8±0.3 | 4.2±0.2 | 4.1±0.3 | 3.0±0.3 | 2.1±0.2 | 2.0±0.2 |
| | 5.0±0.6 | 4.3±0.5 | 4.1±0.5 | 3.1±0.4 | 2.2±0.3 | 2.2±0.3 |
| ¹⁷ N | 24–76 | 22–92 | 20–76 | 18–84 | 18–52 | 16–44 |
| | 2.5±0.3 | 1.6±0.1 | 1.6±0.2 | 1.3±0.2 | 0.9±0.1 | 1.0±0.1 |
| | 2.8±0.4 | 1.6±0.2 | 1.6±0.2 | 1.3±0.2 | | |
| ¹⁵ O | 24–108 | 24–100 | 22–92 | 22–52 | 16–56 | 20–40 |
| | 2.5±0.3 | 1.4±0.1 | 1.3±0.2 | 1.3±0.2 | 1.1±0.1 | 0.5±0.1 |
| ¹⁶ O | 14–108 | 14–100 | 14–100 | 14–84 | 14–76 | 14–60 |
| | 24.8±1.1 | 16.2±0.4 | 12.8±0.7 | 11.4±0.6 | 8.3±0.3 | 7.8±0.4 |
| | 24.9±2.7 | 16.2±1.7 | 12.8±1.5 | 11.4±1.3 | 8.3±0.9 | 7.9±0.9 |
| ¹⁷ O | 18–100 | 14–100 | 16–92 | 16–76 | 16–68 | 16–52 |
| | 11.4±0.6 | 8.9±0.3 | 8.0±0.5 | 5.6±0.4 | 4.3±0.2 | 4.1±0.3 |
| | 11.4±1.3 | 8.9±1.0 | 8.1±1.0 | 5.6±0.7 | 4.4±0.5 | 4.4±0.6 |

TABLE II. (Continued).

| Fragment | 20° | 40° | Angle 60° | 90° | 120° | 160° |
|------------------|-----------|-----------|--------------|-----------|-----------|-----------|
| ¹⁸ O | 22–92 | 20–92 | 20–92 | 18–76 | 18–56 | 18–52 |
| | 7.5±0.5 | 5.6±0.2 | 5.0±0.3 | 3.8±0.3 | 3.0±0.2 | 2.7±0.2 |
| | 7.7±0.9 | 5.7±0.6 | 5.0±0.6 | 4.0±0.5 | 3.2±0.4 | 3.0±0.4 |
| ¹⁹ O | 20–68 | 20–84 | 20–84 | 20–68 | 20–52 | 20–44 |
| | 2.5±0.3 | 1.0±0.1 | 1.5±0.2 | 0.89±0.15 | 0.74±0.10 | 0.41±0.09 |
| ¹⁷ F | 28–52 | 28–60 | 28–60 | 28–52 | 28–60 | 28–44 |
| | 0.36±0.11 | 0.38±0.06 | 0.49±0.12 | 0.20±0.07 | 0.10±0.03 | 0.13±0.04 |
| ¹⁸ F | 28–84 | 18–100 | 24–84 | 24–52 | 22–52 | 20–52 |
| | 3.3±0.3 | 3.7±0.2 | 2.5±0.3 | 1.5±0.2 | 1.2±0.1 | 0.85±0.14 |
| | 3.5±0.8 | 3.8±0.8 | 2.5±0.6 | 1.6±0.4 | 1.3±0.3 | 0.92±0.27 |
| ¹⁹ F | 18–100 | 18–84 | 18–84 | 20–84 | 18–60 | 20–48 |
| | 7.9±0.6 | 6.2±0.3 | 5.5±0.4 | 3.7±0.3 | 3.4±0.2 | 2.2±0.2 |
| | 8.0±1.4 | 6.3±1.0 | 5.6±1.0 | 3.7±0.7 | 3.6±0.6 | |
| ²⁰ F | 26–76 | 24–84 | 20–76 | 24–68 | 18–68 | 22–52 |
| | 5.4±0.4 | 3.8±0.2 | 3.8±0.3 | 2.9±0.3 | 1.8±0.2 | 1.6±0.2 |
| | 5.6±1.3 | 3.9±0.8 | 4.0±0.9 | 3.2±0.8 | 1.8±0.4 | 1.8±0.5 |
| ²¹ F | 26–68 | 24–76 | 28–68 | 22–56 | 18–52 | 20–36 |
| | 2.4±0.3 | 1.3±0.1 | 1.6±0.2 | 1.1±0.2 | 1.1±0.1 | 1.2±0.2 |
| ²² F | 28–36 | 28–60 | 28–52 | 28–60 | 28–44 | 28–44 |
| | 0.09±0.06 | 0.23±0.05 | 0.21±0.08 | 0.20±0.07 | 0.08±0.03 | 0.06±0.03 |
| ¹⁹ Ne | 24–32 | 24–72 | 24–40 | 24–56 | 24–48 | 32–40 |
| | 0.23±0.13 | 0.76±0.12 | 0.32±0.13 | 0.22±0.08 | 0.27±0.07 | 0.11±0.05 |
| ²⁰ Ne | 24–84 | 18–92 | 26–76 | 20–56 | 18–60 | 20–52 |
| | 4.8±0.5 | 4.7±0.3 | 2.3±0.3 | 2.0±0.3 | 2.1±0.2 | 1.4±0.2 |
| | 5.0±1.2 | 4.9±1.1 | 2.5±0.6 | | 2.3±0.6 | 1.4±0.4 |
| ²¹ Ne | 24–92 | 18–92 | 26–76 | 24–76 | 18–60 | 22–60 |
| | 8.6±0.6 | 6.0±0.3 | 3.7±0.3 | 2.9±0.3 | 2.9±0.2 | 1.9±0.2 |
| | 9.1±2.0 | 6.0±1.3 | 4.0±1.0 | 3.2±0.8 | 2.9±0.7 | 1.9±0.5 |
| ²² Ne | 24–92 | 24–84 | 22–76 | 22–68 | 22–60 | 18–48 |
| | 5.8±0.5 | 3.8±0.2 | 3.9±0.4 | 3.3±0.3 | 2.1±0.2 | 2.1±0.3 |
| | 5.9±1.4 | 3.9±0.9 | 4.0±0.9 | 3.7±0.9 | 2.3±0.6 | 2.3±0.6 |
| ²³ Ne | 24–72 | 24–72 | 24–64 | 24–64 | 24–56 | 24–48 |
| | 2.2±0.3 | 1.0±0.1 | 1.1±0.2 | 0.81±0.16 | 0.56±0.09 | 0.62±0.13 |
| ²² Na | 28–68 | 28–92 | 28–52 | 28–52 | 28–60 | 28–36 |
| | 1.5±0.3 | 3.0±0.2 | 1.6±0.3 | 0.96±0.18 | 0.85±0.11 | 0.11±0.06 |
| ²³ Na | 28–84 | 28–84 | 28–76 | 28–76 | 28–76 | 28–52 |
| | 5.7±0.5 | 4.0±0.2 | 3.3±0.3 | 2.0±0.3 | 1.9±0.2 | 1.3±0.2 |
| ²⁴ Na | 28–92 | 28–84 | 28–84 | 28–68 | 28–60 | 28–52 |
| | 3.0±0.4 | 3.2±0.2 | 2.5±0.3 | 2.0±0.3 | 1.3±0.1 | 1.0±0.2 |
| ²⁵ Na | 28–76 | 28–76 | 28–68 | 28–68 | 28–52 | 28–36 |
| | 1.7±0.3 | 1.3±0.1 | 1.3±0.2 | 0.70±0.15 | 0.58±0.10 | 0.54±0.12 |

TABLE II. (Continued).

| Fragment | 20° | 40° | Angle 60° | 90° | 120° | 160° |
|------------------|--------------------|--------------------|--------------------|--------------------|--------------------|------|
| ²⁶ Na | 28–44 0.46±0.17 | 28–68 0.33±0.08 | 28–44 0.48±0.15 | 28–44 0.41±0.12 | 28–44 0.12±0.05 | |
| ²⁴ Mg | 28–84 3.6±0.4 | 28–84 2.8±0.2 | 28–68 1.9±0.3 | 28–68 1.6±0.3 | 28–60 0.87±0.13 | |
| ²⁵ Mg | 28–92 4.5±0.5 | 28–92 3.0±0.2 | 28–68 1.5±0.2 | 28–60 1.1±0.2 | 28–68 1.7±0.2 | |
| ²⁶ Mg | 28–76 4.9±0.5 | 28–76 1.7±0.2 | 28–76 2.5±0.3 | 28–60 1.6±0.2 | 28–60 0.83±0.12 | |
| ²⁷ Mg | 28–68 3.0±0.5 | 28–68 0.73±0.11 | 28–68 0.71±0.18 | 28–68 0.75±0.17 | 28–44 0.17±0.06 | |

momentum. These features allow reasonable interpolations and extrapolations to be made for many of the data sets measured. For example, the third entries in Tables I and II are taken from these individual-spectra, two-component fits. Attempts to ascribe physical significance to the second-component parameters of these fits are most likely inappropriate.

Figure 5 shows the results of applying this procedure to the ¹²C fragment data. The combined component fits and the evaporative contribution are shown for each angle. The contribution from evaporation is small for this case, as is true for all but the light fragments in this study.

B. Invariant cross section analysis

From the smooth fits described in Sec. IV A, sets of points in the $(y, p_{\perp}/mc)$ plane at which the invariant cross sections $(1/p)(d^2\sigma/dE d\Omega)$ are identical can easily be extracted. Here $y = \tanh^{-1}\beta_{\parallel}$ and p_{\perp} , are, respectively, the fragment's rapidity and transverse momentum; for fragment rest mass energies mc^2 much larger than their kinetic energies (as for all the work here), y and p_{\perp}/mc approach, respectively, the fragment's parallel and perpendicular velocities β_{\parallel} and β_{\perp} . These sets of points then allow an extension of analysis of the form described in Ref.

TABLE III. The range of measurements made using $\Delta E, E$ particle identification for compact detector telescopes and approximately 0.2 mg/cm² Ag targets. Fragments are separated only in Z and values given are integrated over all fragment masses. The meanings of the entries are described in the caption for Table I.

| Fragment | 20° | 40° | Angle 60° | 90° | 120° | 160° |
|----------|--------------------|--------------------|--------------------|--------------------|-------------------|-------------------|
| B | 18–124 212±4 | 18–124 156±3 | 20–116 135±3 | 12–108 110±2 | 12–92 82±1 | 14–84 52±1 |
| C | 18–124 172±3 | 18–124 113±2 | 18–124 99±3 | 16–116 91±1 | 16–84 67±1 | 16–68 49±1 |
| N | 20–108 68.2±1.5 | 20–100 44.2±1.0 | 20–108 40.7±0.8 | 20–84 33.8±0.5 | 20–68 24.9±0.5 | 20–60 17.8±0.4 |
| O | 22–100 44.0±1.2 | 22–100 32.1±0.7 | 22–92 26.5±0.5 | 22–100 21.5±0.4 | 22–76 15.2±0.4 | 22–68 10.3±0.3 |
| F | 26–92 19.0±0.8 | 26–100 14.2±0.5 | 26–92 11.6±0.4 | 26–84 9.2±0.3 | 26–68 6.5±0.3 | 26–56 3.4±0.2 |
| Ne | 28–92 18.0±0.8 | 28–100 13.8±0.5 | 28–92 11.7±0.4 | 28–76 8.7±0.3 | 28–68 5.3±0.2 | 28–68 2.8±0.1 |
| Na | 32–92 13.4±0.7 | 32–92 10.8±0.4 | 32–84 8.0±0.3 | 32–76 6.0±0.2 | 32–56 3.5±0.2 | 32–60 1.9±0.1 |

2. This type of analysis, itself a refinement of an earlier technique used in a relativistic heavy ion study,¹⁹ has subsequently been used in several different kinds of studies in which statistical mechanisms were thought to be of possible importance, e.g., Refs. 3 and 20–24. In this subsection, we discuss the applications of such analysis to our data for all fragment energies above 30 MeV where the analysis is less sensitive to relative normalization than at lower fragment energies.

Figures 6–8 show examples of data displayed in this manner. The contour levels shown are two-parameter, least-squares fits to the points which they intersect and are merely circles centered on the rapidity axis. Each such fit corresponds to isotropic emission from a moving source. The two parameters describing each contour can thus be taken as β_s , an effective source velocity giving the position of the circle's center, and β_r , an effective radial velocity giving the circle's radius. The word effective is used to stress that no physically meaningful description of

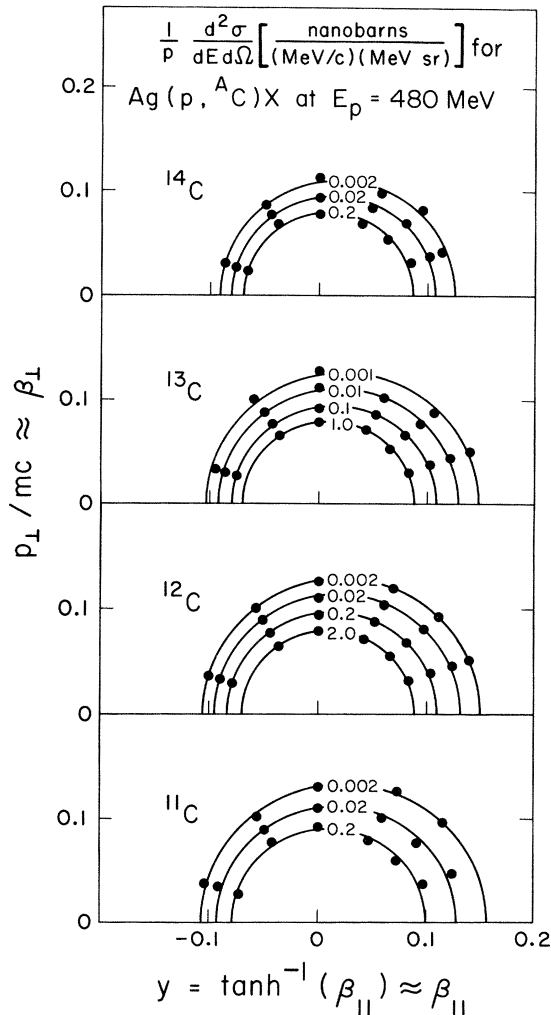


FIG. 6. Sets of data points of constant invariant cross section for various mass carbon fragments from 480 MeV protons incident on Ag. Fits for isotropic emission from sources moving in the beam direction are also shown. The displacements of the data points from the contour lines corresponding to these fits have been exaggerated by a factor of approximately 3.

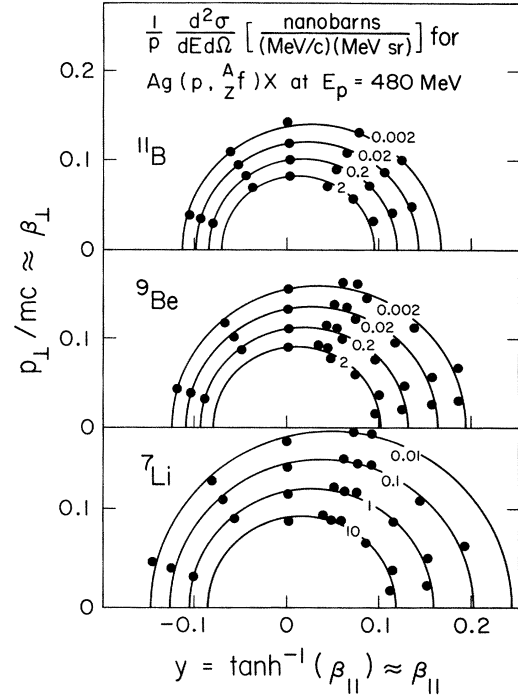


FIG. 7. Constant invariant cross section data points for three $A = (2Z + 1)$ fragments. See Fig. 6 caption for a description of the details.

the fragment emission process is necessarily implied by these fits. Data points are included in the analysis only if they are interpolated points, i.e., within the range of energies actually observed in the measurements at the given angle.

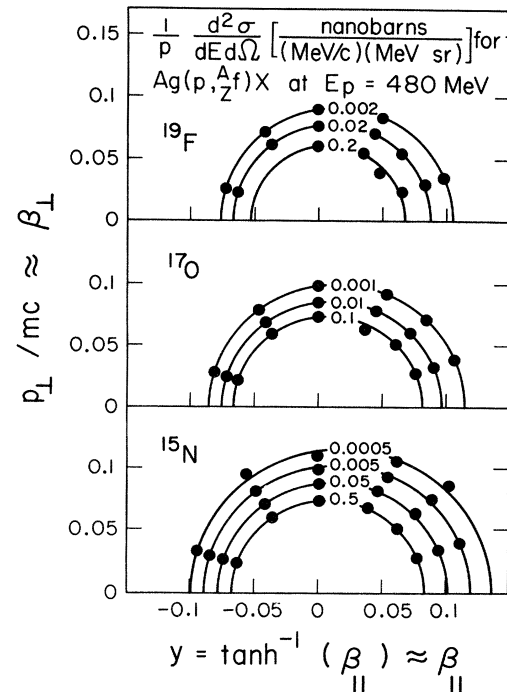


FIG. 8. Same as Fig. 7 for three higher mass fragments.

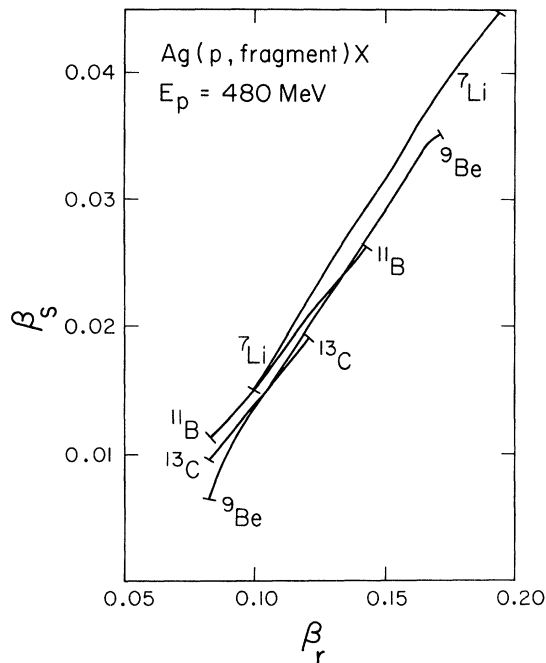


FIG. 9. Effective source velocity versus effective fragment radial velocity for selected cases from Figs. 6 and 7.

While no physical model has been implied, the extremely good fits achieved in this type of analysis certainly merit further consideration. When the β_s and β_r values are investigated, the striking relation between them previously noted for less extensive data sets^{3,15} is found to hold over the entire expanded data set being discussed here. Figure 9 illustrates this relation for some of the cases shown in Figs. 6 and 7. Curves in Fig. 9 are terminated when less than five data points determine the isotropic emission fits. The variation between fragments is typical of what is seen when other fragment data are plotted on such a graph. To a remarkable level, one sees a linear relation between β_s and β_r that is virtually identical for all emitted fragments.

Obviously, fragment emission is much too complicated a process for one to be able to associate a given invariant cross section with a specific source limited to a single velocity. However, it appears that when one integrates over the various possible sources which may give rise to fragments, in lowest order one can describe the average systematics in very simple terms, namely that fragments appear to be emitted isotropically from sources whose velocities are directly related to the fragment velocities in the emitting system's rest frame. The relation appears nearly linear and universal over the range of fragment velocities studied here.

C. Nonevaporative component fits encompassing a fragment's global kinematic range

If one wants to consider statistical emission of fragments from moving sources, the analysis in Sec. IV B places strong constraints on any simple form chosen. In this subsection, we attempt to choose the simplest such

model which will fit the spectra of a given fragment type over all emission angles and energies.

Clearly one begins with the kinematics dictated by the data, i.e., a linear relationship

$$\beta_s = a + b\beta_r \quad (4)$$

between the source velocity β_s and the fragment radial velocity β_r in the rest frame of the source. The parameters a and b could be fixed on the basis of graphs such as Fig. 9, but we use them as free parameters in the chi-squared fits discussed here because we can then obtain a measure of the degree of universality in this relationship.

This type of relationship between source velocity and fragment radial velocity has been used before.^{11,16,25} A preconceived idea of the form of the correlation between β_s and β_r in the earlier studies^{11,16} resulted in the use of a constrained parametrization of the relationship and is probably one reason the fits obtained were not considered

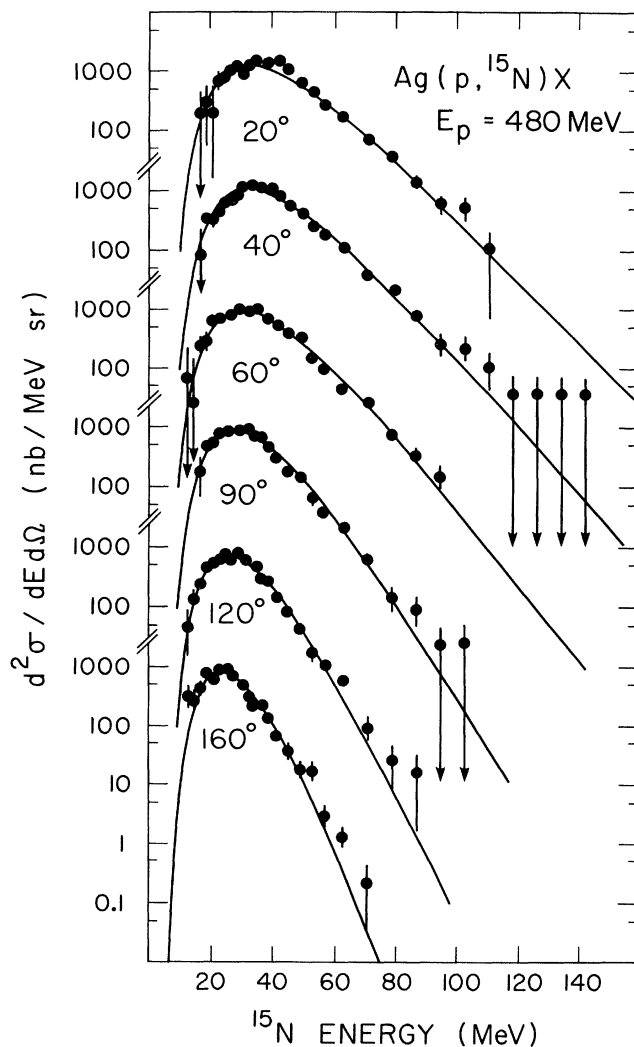


FIG. 10. Energy spectra of ^{15}N fragments at six laboratory angles. The curves shown are generated for all angles using only one set of values in the six-parameter functional form described in Sec. IV C.

good by the authors. When the parameters a and b of Eq. (4) were determined²⁵ from data, it was reported that reasonable fits to various nucleus-nucleus and proton-nucleus fragment emission data were obtained.

For our description of emission in the frame of the source, we use a simple falling exponential times a function chosen to approximate an inverse cross section. For the latter function, we chose a form derived from a Fermi distribution in the reciprocal of the fragment energy. Such a form gives zero cross section at zero energy and allows control of the position and spectrum width near the most probable fragment energy. The choice of energy (rather than say momentum) was made mainly to facilitate comparison of results with thermal-type models (momentum was used for individual angle fits discussed earlier). The actual parametrization used is

$$\left(\frac{d^2\sigma}{d\Omega dE} \right)_{\text{source frame}} = A e^{-E/\tau} \left[1 + \left(\frac{x}{1-x} \right) e^{M(M-E)/x\tau E} \right]^{-1} \quad (5)$$

which, with Eq. (4), yields a total of six parameters: a , b , A , τ , x , and M . This form is used since τ and M are readily interpreted. In the source frame, M is the most probable value for fragment energy and τ characterizes the exponential falloff at large fragment energies. The parameter x controls the width of the energy distribution near M , and A controls the overall normalization; A and

x are strongly coupled to the values of other parameters and have no simple direct interpretation.

For the higher Z fragments where standard evaporation contributions are small, we can use this parametrization by itself to obtain very reasonable fits to the data. Figure 10 shows an example for ^{15}N fragments. When the statistical errors only are used in the fits, the reduced chi-squared values obtained for these heavier fragments are typically around 2. This indicated lack of precision in the fits may be due to a slightly imperfect functional form and/or to neglecting relative errors between angles. This is considered further in Sec. IV D.

One great advantage to a functional form valid for all angles is illustrated in Fig. 11 where this form has been fitted to the ^{24}Na fragment data. In this case, as with all of the Na and Mg fragments and with the lower-yield O through Ne isotopes, the data at any given angle were insufficient to define parameters for the individual angle fits described earlier. However, when data from all angles can be used as input, the six parameters of the global fit are determined quite readily. This makes it possible to estimate total production cross sections easily and directly using the fits.

D. Combined evaporative and global nonevaporative fits

For our lighter fragments, the function described in Sec. IV C does not yield good fits until the evaporative component is taken into account. To incorporate this component in our fitting procedure, we adopted the following strategy. The two principal parameters in the evaporation calculation of Ref. 14, β and E_M^* , were adjusted (only small changes from values reported there resulted) until the best simultaneous fits including both evaporation and the global nonevaporative components were obtained for ^4He and ^9Be . Subsequent evaporation calculations were done using these fixed values for β and E_M^* . The calculated evaporative components were then included with the global nonevaporative fits with only their relative overall normalizations allowed to vary, thus giving a seven parameter fit to any given fragment.

In doing these fits, it was clear that the errors used needed to account for uncertainties in relative normalization between angles since these were obviously significantly larger than the statistical errors for much of the lighter fragment data. However, when our quoted 10% value was included with the statistical errors, the reduced chi-squared values were unreasonably small and the parameters which resulted fitted the exponential tails very well at the expense of fitting the mean overall magnitude (inappropriate for fits used to determine total cross sections). It was empirically determined that an error of 5% of $d^2\sigma/dE d\Omega$ added in quadrature with the statistical error gave good results when used in these fits and this prescription was followed.

Such combined-component, all-angle fits are illustrated in Figs. 12 and 13 for ^7Li and ^7Be fragments. The auxiliary measurements at 65° and 70° were made to verify the previously noted absence of obvious quasifree scattering effects. Recoil energies for $A=7$ fragments elastically scattered in interactions with 480 MeV protons are indi-

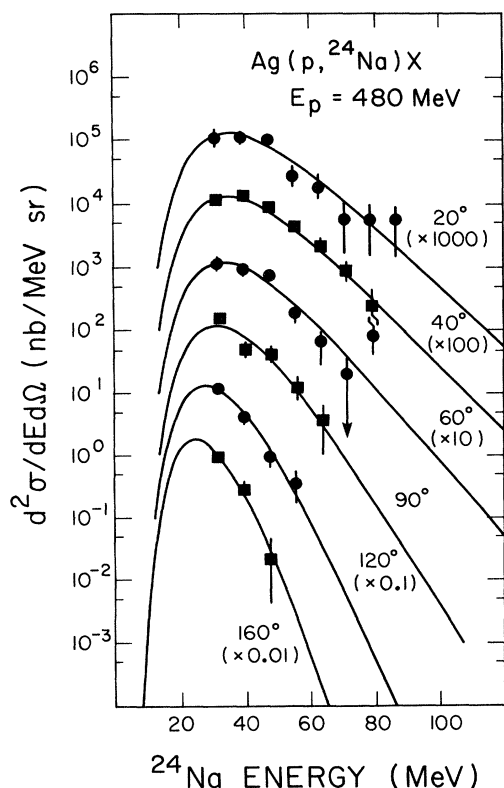


FIG. 11. Energy spectra of ^{24}Na fragments at six laboratory angles. The six-parameter fit described in Sec. IV C is also shown.

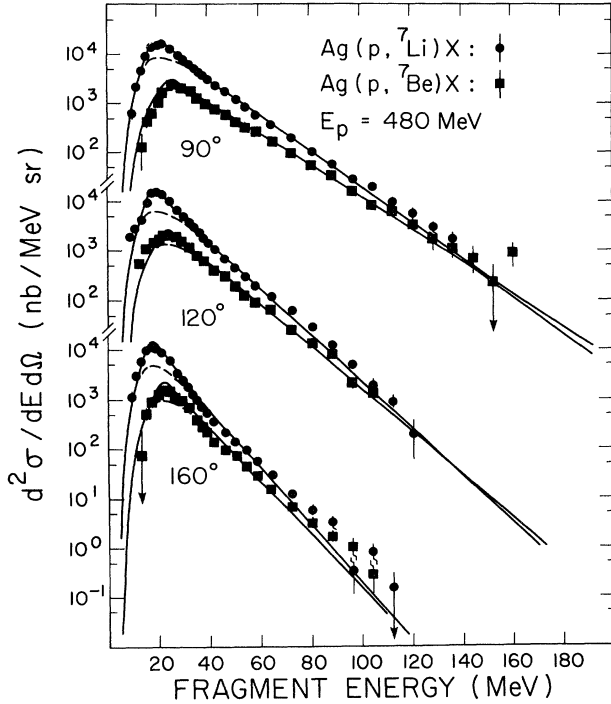


FIG. 12. Energy spectra of ${}^7\text{Li}$ and ${}^7\text{Be}$ fragments at 90° , 120° , and 160° laboratory angles. The dashed curves indicate the global nonevaporative portion (Sec. IV C) of the combined component fits of Sec. IV D. The solid curves are the total fits when the evaporative component is included.

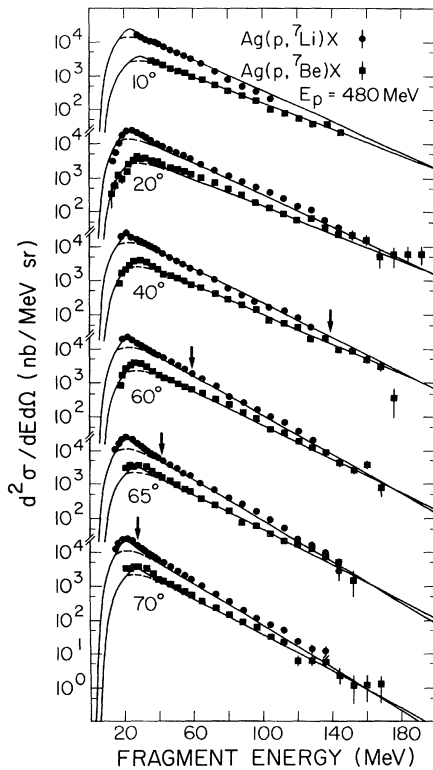


FIG. 13. Energy spectra of ${}^7\text{Li}$ and ${}^7\text{Be}$ fragments at six forward laboratory angles. The curves are as described for Fig. 12. Also indicated by arrows are the energies which an $A=7$ nucleus would have if recoiling from elastic scattering of a 480 MeV proton.

cated in Fig. 13. No notable deviations from our fits are discernible around these values.

E. Extracted parameters and total cross sections

Examples of angular distributions for energy-integrated spectra $d\sigma/d\Omega$ are given in Fig. 14. The extrapolated values from the third entries in Tables I and II are used, but the errors shown (and used in determining the fits shown for exponentials in $\cos\theta$) are the smaller values obtained by using a 5% error for relative cross section added in quadrature with the statistical error (as in Sec. IV D) and with a 30% error in the extrapolated contribution. Using the fits shown to the angular distributions, the angular integrations are readily done to find fragment total cross sections. Values found by this means are tabulated in Table IV under the heading of "measured σ " (only minor contributions from the energy extrapolations introduce direct nuclear model dependence). No such entry is made where individual fragment energy spectra are not sufficiently well determined to define reasonable fits of the type discussed in Sec. IV A. The uncertainties quoted for these numbers are not overall errors but rather reflect only the accuracies with which the normalizations of the fits to the angular distributions are determined within the prescription used.

The remaining entries in Table IV are taken from the fits described in Sec. IV D. Where we have been able to calculate total cross sections by the means described in the preceding paragraph, the values found agree well with the tabulated total σ from these fits. The contributions to σ

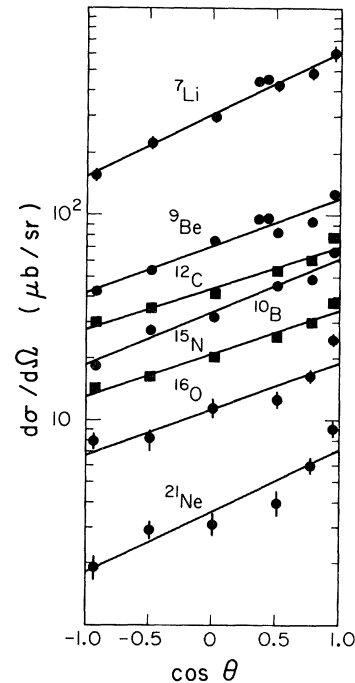


FIG. 14. Laboratory angular distributions for energy-integrated cross sections. Errors shown are the relative values used as input in the procedure that determined the indicated fits in exponentials of $\cos\theta$. These fits were subsequently used to integrate the data over angle.

TABLE IV. Total primary production cross sections calculated assuming an exponential angular dependence on $\cos\theta$. The entries labeled “measured σ ” are calculated by means described in the text and have no substantive dependence on nuclear models; errors quoted in these entries are not the overall values but rather only a measure of the accuracy with which the technique used for integration can be applied to the data. The remaining entries for each fragment are values from the fits described in Sec. IV D where the evaporative component has been combined with the global nonevaporative fits of Sec. IV C. They are discussed in more detail in the text.

| | Measured | Total | σ (μb) | Global Angular Fit | | Nonevaporative | τ |
|-----------------------------|----------------------------|---------|----------------------------|--------------------|------------------------------|----------------|--------|
| | σ (μb) | | | Evaporative | Norm | | |
| ^3He | 35 300 ^a | 34 200 | 6 400 | 19 | 1.6 \pm 0.08 | 27 800 | 23.9 |
| ^4He | 453 000 ^a | 444 000 | 282 000 | 64 | 1.0 \pm 0.004 ^c | 162 000 | 14.4 |
| ^6Li | 3 720 \pm 70 | 3 670 | 910 | 25 | 1.3 \pm 0.05 | 2 760 | 14.9 |
| ^7Li | 4 240 \pm 80 | 4 200 | 1 160 | 27 | 1.7 \pm 0.04 | 3 040 | 12.6 |
| $^8\text{Li}^{\text{b}}$ | | 448 | | | | 448 | 12.5 |
| $^9\text{Li}^{\text{b}}$ | | 69.8 | | | | 69.8 | 13.5 |
| ^7Be | 841 \pm 17 | 836 | 139 | 17 | 1.5 \pm 0.07 | 697 | 14.4 |
| ^9Be | 932 \pm 18 | 922 | 164 | 18 | 1.0 \pm 0.04 ^c | 758 | 9.6 |
| ^{10}Be | 418 \pm 8 | 416 | 70 | 17 | 0.8 \pm 0.05 | 346 | 10.0 |
| $^{11}\text{Be}^{\text{b}}$ | | 12.9 | | | | 12.9 | 16.7 |
| ^{10}B | 450 \pm 11 | 485 | 75 | 15 | 1.2 \pm 0.1 | 410 | 10.9 |
| ^{11}B | 842 \pm 19 | 862 | 119 | 14 | 1.2 \pm 0.09 | 743 | 9.4 |
| ^{12}B | 121 \pm 3 | 118 | 8 | 8 | 0.5 \pm 0.1 | 109 | 8.4 |
| ^{13}B | 20.5 \pm 0.9 | 18.5 | 2.3 | 12 | 0.5 \pm 0.2 | 16.2 | 7.0 |
| ^{11}C | 88.1 \pm 3.0 | 96.5 | 15.0 | 16 | 1.1 \pm 0.1 | 81.5 | 9.4 |
| ^{12}C | 574 \pm 13 | 561 | 57 | 10 | 0.9 \pm 0.1 | 504 | 7.8 |
| ^{13}C | 394 \pm 9 | 386 | 32 | 8 | 0.7 \pm 0.1 | 354 | 7.5 |
| ^{14}C | 139 \pm 4 | 131 | | | | 131 | 6.7 |
| ^{14}N | 143 \pm 4 | 138 | 10 | 7 | 0.9 \pm 0.2 | 128 | 7.0 |
| ^{15}N | 275 \pm 7 | 270 | 9 | 3 | 0.5 \pm 0.2 | 261 | 6.4 |
| ^{16}N | 39.5 \pm 1.6 | 38.0 | | | | 38.0 | 6.2 |
| ^{17}N | 16.0 \pm 2.2 | 15.2 | | | | 15.2 | 5.4 |
| ^{15}O | | 14.3 | 1.6 | 11 | 1.4 \pm 0.4 | 12.7 | 7.7 |
| ^{16}O | 149 \pm 4 | 137 | 3 | 2 | 0.7 \pm 0.4 | 134 | 6.4 |
| ^{17}O | 80.4 \pm 2.7 | 75.0 | | | | 75.0 | 5.5 |
| ^{18}O | 54.1 \pm 2.1 | 49.7 | | | | 49.7 | 5.4 |
| ^{19}O | | 11.3 | | | | 11.3 | 5.3 |
| ^{17}F | | 4.0 | | | | 4.0 | 5.0 |
| ^{18}F | 25.4 \pm 1.4 | 23.3 | | | | 23.3 | 6.7 |
| ^{19}F | 56.4 \pm 2.8 | 50.2 | 1.1 | 2 | 0.8 \pm 0.9 | 49.1 | 6.1 |
| ^{20}F | 36.6 \pm 1.6 | 33.1 | 0.4 | 1 | 0.4 \pm 1.2 | 32.7 | 5.3 |
| ^{21}F | | 14.9 | 1.0 | 7 | 4.4 \pm 2.7 | 13.9 | 5.5 |
| ^{22}F | | 3.2 | | | | 3.2 | 3.8 |
| ^{19}Ne | | 4.0 | | | | 4.0 | 4.9 |
| ^{20}Ne | 34.4 \pm 2.0 | 28.8 | | | | 28.8 | 6.0 |
| ^{21}Ne | 48.3 \pm 2.1 | 46.6 | | | | 46.6 | 6.0 |
| ^{22}Ne | 40.9 \pm 1.9 | 36.1 | | | | 36.1 | 5.0 |
| ^{23}Ne | | 12.7 | | | | 12.7 | 6.1 |
| ^{22}Na | | 19.1 | | | | 19.1 | 6.7 |
| ^{23}Na | | 40.7 | | | | 40.7 | 4.4 |
| ^{24}Na | | 34.2 | | | | 34.2 | 4.9 |
| ^{25}Na | | 17.0 | | | | 17.0 | 4.8 |

TABLE IV. (Continued).

| Measured σ (μb) | Total σ (μb) | σ (μb) | Global Angular Fit | | Nonevaporative σ (μb) | τ |
|--|-------------------------------------|----------------------------|--------------------|------|--|--------|
| | | | Evaporative % | Norm | | |
| ^{24}Mg | 20.5 | | | | 20.5 | 4.3 |
| ^{25}Mg | 22.6 | | | | 22.6 | 3.6 |
| ^{26}Mg | 19.4 | | | | 19.4 | 5.6 |
| ^{27}Mg | 6.1 | | | | 6.1 | 6.5 |

^aValues from Ref. 3.

^bDue to a lack of low energy experimental points needed to determine the maximum and width parameters of the fit, the values have been restricted to lie within the range determined for the other isotopes of the element. No evaporation component has been subtracted.

^cValues of 1.0 used in determining evaporation parameters.

from both components in this fit are tabulated separately, and the percentage due to the conventional evaporation component is given for those cases where this component is included in the fit. In general, this contribution decreases as the fragment Z increases, becoming eventually a small contribution with a large uncertainty relative to its size. These uncertainties are indicated by the entries for the evaporation component "norm." The norm entry is the fraction of the absolutely normalized evaporation calculation required by the fitting procedure of Sec. IV D in order to minimize chi-squared. The accuracy to which this parameter is determined by the fitting procedure is the indicated uncertainty in each of these entries.

In the fitting procedure of Sec. IV D the evaporation calculation parameters were determined by requiring that the norms for ^4He and ^9Be simultaneously be unity. The remaining norms were then determined using these fixed evaporation parameters. These norm values are very reasonable, especially in light of the indicated errors, and suggest that we have been able within a factor of less than 2 to calculate absolutely and self-consistently the evaporation components in these spectra. The calculation¹⁴ takes into account only particle stable states of the emitted fragments, and a preliminary examination indicates that branching from the decay of fragments emitted in particle unstable states might improve on this already surprisingly good result. However, the predominance of the nonevaporative components makes such efforts difficult and of limited interest.

As anticipated on the basis of Fig. 9 and similar results, the values for the parameters a and b of Eq. (4) in the global nonevaporative component showed little variation from fragment to fragment. This is perhaps best illustrated by the means and standard deviations $a = -0.020 \pm 0.005$ and $b = 0.35 \pm 0.06$ of the a and b values from the fits to the 28 fragments with measured σ entries. (Using values from fits for all cases with entries in Table IV yields $a = -0.021 \pm 0.007$ and $b = 0.38 \pm 0.12$, but these values are clearly distorted by a few cases where poor statistical accuracy has not allowed accurate parameter definition.) Even within the narrow range indicated by the standard deviations in the a and b values, it is possible to discern slight trends with fragment mass A_f . The values for a appear to be increasingly negative with increasing A_f , while the values for b tend to be increasingly positive

with A_f . Since the fragments of higher A_f sample mainly smaller values of β_r , one interpretation of these trends is that the relationship between β_s and β_r may still be nearly universal, but that it is not linear over its entire range.

The final entries for the combined component fits in Table IV are the values τ characterizing the exponentially falling part of the nonevaporative component. With a few exceptions, often apparently related to statistical accuracy, the general trend is for τ to decrease with increasing fragment Z and for τ to decrease with increasing A_f for fixed Z . For $Z > 6$, however, these trends flatten and variations in τ are mainly confined within a reasonably small neighborhood. The somewhat similar values of τ at higher fragment Z might encourage consideration of some form of a universal statistical mechanism as giving rise to these fragments, but it is clearly more difficult to incorporate the lighter fragments into any such picture. In particular, ^7Li and ^7Be have essentially identical kinematics but have τ values which differ by significantly more than the errors in their determinations, as one would expect merely by comparing their spectra in Figs. 12 and 13. Thus it appears that the nonevaporative components differ significantly from fragment to fragment when one attempts to view them as some form of statistical process. This is troublesome for any thermal model interpretation of fragment spectra.

For some models of fragment production, knowledge of the isobaric fragment yields is important. For example, such data from this study have already been used in connection with the snowball model.⁷ More recently, such data from a higher energy study have been used to suggest that fragments may be formed by statistical clustering near the critical point for the phase transition from an energetic collection of free nucleons to nuclear matter.²⁶ In this model, one expects and finds at the higher energies (with some anomalies from isobars with limited particle stable members) that the isobaric yields follow a power law $A_f^{-\eta}$ in the fragment mass. We have examined our data in light of this expectation in Fig. 15. Mass $A_f=6$ has been excluded because we have not measured ^6He and mass $A_f=8$ has been excluded since its contributing members are all in the low-yield wings for their respective atomic numbers. Masses $A_f=13, 14,$ and 15 have been increased by 20, 10, and 40 μb to account for our esti-

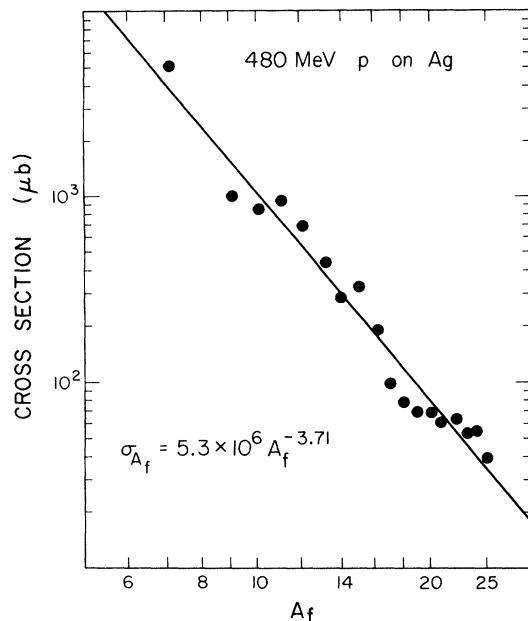


FIG. 15. Total isobaric cross sections and a least-squares power law fit to them.

mates from yield systematics for the ^{13}N , ^{14}B , and ^{15}C members. Our power law fit, of comparable quality to that of Ref. 26 in this A_f mass range, yields a value $\eta=3.71$. This is significantly outside the range of $2 \leq \eta \leq 3$ expected for a distribution resulting from condensation at the critical point, but this is not surprising since it is hard to imagine a 480 MeV proton being able to heat an Ag nucleus to this critical point. A detailed version of the model²⁷⁻²⁹ allowing its extension to regions other than the critical point has recently been applied²⁹ to intermediate energy p + Ag reactions to describe the isobaric mass yields and average spectrum temperatures. However, the physical assumptions implicit in this model may not be compatible with those derived from other considerations.³⁰

V. SUMMARY AND CONCLUSIONS

This paper has presented results¹ on Ag(p,fragment) inclusive spectra whose ultimate utility may await future advances in the theory of fragment emission. Within the limits of the analyses presented, several conclusions can be based on the data, as discussed at various points throughout the paper. We close with a summary of some of the more salient points.

From the purely experimental side, it is worth noting that standard silicon detector technology can be used with time-of-flight determinations to measure isotopically resolved fragment energy spectra at energies down to nearly 1 MeV/nucleon for fragment Z up to at least 12. Multiple scattering in the ΔE counter will introduce significant corrections, but these can be well determined by a combination of measurement and multiple scattering theory. More complex experimental techniques such as gas ΔE counters or timing using parallel plate avalanche

detectors are required only for energy determinations below 1 MeV/nucleon or for fragment Z beyond approximately ten.

As has become increasingly evident during the last decade, fragment spectra from proton induced reactions are not predominantly governed by the processes described in the standard evaporation theory for fully equilibrated residual nuclei. Such evaporation components, which must in fact exist to some extent for all fragments since they clearly exist for ^4He , cannot be totally neglected, but it would appear they are relatively minor contributions to the spectra of fragments heavier than ^4He . Our calculations indicate such contributions at approximately 25% of the total yield for Li fragments decreasing to a few percent of the yield for fragments beyond oxygen.

Analysis of invariant cross section contour levels in the plane of rapidity and perpendicular momentum indicates a nearly universal kinematic relationship for all emitted fragments. All contours appear to be characterized by two parameters, an effective source velocity β_s and an effective fragment radial velocity β_r . The relation between β_r and β_s (approximately $\beta_s = -0.02 + 0.35\beta_r$) appears to be nearly identical for all fragments in the regions where standard evaporation contributions are negligible.

By combining the kinematic relationship found in the invariant cross section analysis with a four-parameter functional form appropriate for isotropic emission from a moving statistical source, the nonevaporative part of the spectra for any given fragment could be simultaneously fit at all emission angles. Coupled with minor variations between fragments in the normalization of our calculation for the evaporative component, this procedure yielded reasonable overall fits to 46 fragment species. However, although the nonevaporative form used is similar to typical thermal models, the variation of the temperaturelike parameter with fragment-type suggests that this is probably not a valid physical interpretation. The origin of the universal relation between β_s and β_r , while currently a puzzle for any model, may in particular trouble thermal models, as pointed out in Ref. 15.

Direct knockout models, on the other hand, also find little support from the data. In particular, the quasistatistical fits summarized in the previous paragraph simultaneously fit the data well in all kinematic regions including those one would expect to be enhanced by contributions from quasifree scattering between the incident proton and clusters with the mass of the observed fragment.

While a model based on liquid-gas phase transitions in nuclear systems shows promise in explaining isobaric yields in the data reported here,²⁹ such models have not yet been extended to explain the observed variations in fragment spectra with emission angle. There also exist alternate explanations of the properties described by this model.^{30,31}

In conclusion, while analysis of the data presented here has provided a relatively simple way to describe a fragment's inclusive spectra over a broad kinematic range encompassing all emission angles, this description has not yet resulted in any obviously better physical understanding of the nonevaporative components in these spectra. However, it is hoped that the extensive experimental char-

acterization of Ag(p,fragment) inclusive spectra now available will help lead to such an improved physical understanding at some point in the future.

ACKNOWLEDGMENTS

The authors wish to thank A. Kurn for his many contributions in the design and implementation of the computer programs used—especially the on-line computer controlled data acquisition system—and for his assistance during experimental data collection. For analysis of the large volumes of data involved, we are indebted to C. R.

Toren for his programming efforts. We greatly appreciate the work of N. Bohna in processing the data through the Simon Fraser University Computing Centre and in compiling and checking the extensive data tabulations associated with this paper. Timely and accurate work from the Simon Fraser University Science Machine Shop under the direction of F. Wick has been a valuable asset in mounting this experimental program. We acknowledge with thanks the help received from the operations staff of TRIUMF in obtaining the proton beams used in this experiment. This work was supported by the Natural Sciences and Engineering Research Council of Canada.

- ¹See AIP document PRVC17-29-1806-65 for 65 pages of numerically tabulated histograms of the single particle inclusive spectra discussed in this article. Order by PAPS number and journal reference from American Institute of Physics, Physics Auxiliary Publication Service, 335 E. 45 St., New York, N.Y. 10017. The price is \$1.50 for microfiche, or \$10.05 for photocopies. Airmail additional. Make check payable to American Institute of Physics.
- ²R. E. L. Green and R. G. Korteling, *Phys. Rev. C* **18**, 311 (1978).
- ³R. E. L. Green and R. G. Korteling, *Phys. Rev. C* **22**, 1594 (1980).
- ⁴R. E. L. Green, K. P. Jackson, and R. G. Korteling, *Phys. Rev. C* **25**, 828 (1982).
- ⁵D. H. Boal and R. M. Woloshyn, *Phys. Rev. C* **20**, 1878 (1979).
- ⁶D. H. Boal and R. M. Woloshyn, *Phys. Rev. C* **23**, 1206 (1981).
- ⁷D. H. Boal, R. E. L. Green, R. G. Korteling, and M. Soroushian, *Phys. Rev. C* **23**, 2788 (1981); D. H. Boal and M. Soroushian, *ibid.* **25**, 1003 (1982).
- ⁸D. H. Boal, Los Alamos Laboratory Report No. LA-8835-C, 1980.
- ⁹S. Frankel, W. Frati, M. Gazzaly, G. W. Hoffman, O. Van Dyck, and R. M. Woloshyn, *Phys. Rev. Lett.* **41**, 148 (1978).
- ¹⁰G. Roy, L. G. Greeniaus, G. A. Moss, D. A. Hutcheon, R. Lijstrand, R. M. Woloshyn, D. H. Boal, A. W. Stetz, K. Aniol, A. Willis, N. Willis, and R. McCamis, *Phys. Rev. C* **23**, 1671 (1981).
- ¹¹E. K. Hyde, G. W. Butler, and A. M. Poskanzer, *Phys. Rev. C* **4**, 1759 (1971).
- ¹²G. D. Westfall, R. G. Sextro, A. M. Poskanzer, A. M. Zebelman, G. W. Butler, and E. K. Hyde, *Phys. Rev. C* **17**, 1368 (1978).
- ¹³J. R. Wu, C. C. Chang, and H. D. Holmgren, *Phys. Rev. C* **19**, 698 (1979).
- ¹⁴R. E. L. Green and R. G. Korteling, *Nucl. Instrum. Methods* **185**, 195 (1981).
- ¹⁵P. B. Price and J. Stevenson, *Phys. Lett.* **78B**, 197 (1978).
- ¹⁶A. M. Poskanzer, G. W. Butler, and E. K. Hyde, *Phys. Rev. C* **3**, 882 (1971).
- ¹⁷A. G. Seamster, R. E. L. Green, and R. G. Korteling, *Nucl. Instrum. Methods* **145**, 583 (1977).
- ¹⁸See, for example, J. D. Jackson, *Classical Electrodynamics*, 2nd ed. (Wiley, New York, 1975), pp. 643–651, or references cited therein.
- ¹⁹J. Gosset, H. H. Gutbrod, W. G. Meyer, A. M. Poskanzer, A. Sandoval, R. Stock, and G. D. Westfall, *Phys. Rev. C* **16**, 629 (1977).
- ²⁰S. Nagamiya, L. Anderson, W. Bruckner, O. Chamberlain, M.-C. Lemaire, S. Schnetzer, G. Shapiro, H. Steiner, and I. Tanihata, *Phys. Lett.* **81B**, 147 (1979).
- ²¹A. Sandoval, H. H. Gutbrod, W. G. Meyer, R. Stock, Ch. Lukner, A. M. Poskanzer, J. Gosset, J.-C. Jourdain, C. H. King, G. King, N. V. Sen, G. D. Westfall, and K. L. Wolf, *Phys. Rev. C* **21**, 1321 (1980).
- ²²R. D. McKeown, S. J. Sanders, J. P. Schiffer, H. E. Jackson, M. Paul, J. R. Specht, E. J. Stephenson, R. P. Redwine, and R. E. Segel, *Phys. Rev. Lett.* **44**, 1033 (1980).
- ²³K. L. Wolf, H. H. Gutbrod, W. G. Meyer, A. M. Poskanzer, A. Sandoval, R. Stock, J. Gosset, J.-C. Jourdain, C. H. King, G. King, N. V. Sen, and G. D. Westfall, *Phys. Rev. C* **26**, 2572 (1982).
- ²⁴L. G. Sobotka, M. L. Padgett, G. J. Wozniak, G. Guarino, A. J. Pacheco, L. G. Moretto, Y. Chan, R. G. Stokstad, I. Tserurya, and S. Wald, *Phys. Rev. Lett.* **51**, 2187 (1983).
- ²⁵P. B. Price, J. Stevenson, and K. Frankel, *Phys. Rev. Lett.* **39**, 177 (1977).
- ²⁶J. E. Finn, S. Agarwal, A. Bujak, J. Chuang, L. J. Gutay, A. S. Hirsch, R. W. Minich, N. T. Porile, R. P. Scharenberg, B. C. Stringfellow, and F. Turkot, *Phys. Rev. Lett.* **49**, 1321 (1982).
- ²⁷M. E. Fisher, *Physics (N.Y.)* **3**, 255 (1967).
- ²⁸R. W. Minich, S. Agarwal, A. Bujak, J. Chuang, J. E. Finn, L. J. Gutay, A. S. Hirsch, N. T. Porile, R. P. Scharenberg, B. C. Stringfellow, and F. Turkot, *Phys. Lett.* **118B**, 458 (1982).
- ²⁹A. D. Panagiotou, M. W. Curtain, H. Toki, D. K. Scott, and P. J. Siemens, Michigan State University Cyclotron Laboratory Report MSUCL-433, 1983.
- ³⁰D. H. Boal, Michigan State University Cyclotron Laboratory Report MSUCL-443, 1983.
- ³¹D. H. Boal, *Phys. Rev. C* **28**, 2568 (1983).